Monthly Notices of the ROYAL ASTRONOMICAL SOCIETY

MNRAS **481,** 3063–3069 (2018)
Advance Access publication 2018 September 6

doi:10.1093/mnras/sty2429

Dependence of clustering of X-ray AGN on obscuration

L. Koutoulidis,[1★] I. Georgantopoulos,[1★] G. Mountrichas,[1★] M. Plionis,[1,2] A. Georgakakis,[1,3] A. Akylas[1] and E. Rovilos[1]

[1]*National Observatory of Athens, V. Paulou & I. Metaxa 15236, Penteli, Greece*
[2]*Physics Department, Aristotle University of Thessaloniki, Thessaloniki 54124, Greece*
[3]*Max-Planck-Institut für Extraterrestrische Physik (MPE), Postfach 1312, D-85741 Garching, Germany*

Accepted 2018 August 28. Received 2018 August 22; in original form 2017 July 5

ABSTRACT

Recent studies which select active galactic nucleus (AGN) in the mid-infrared (IR) part of the spectrum find that obscured AGNs reside in more massive dark matter haloes compared to unobscured ones. In contrast, X-ray AGN surveys do not find a difference in the dark matter haloes of these two populations. We visit anew this issue by examining the clustering properties of a large X-ray sample distributed over five deep fields. These are the CDF-N, CDF-S, ECDF-S, COSMOS, and AEGIS *Chandra* fields spanning the redshift interval $0.6 < z < 1.4$. In particular, we present the clustering properties of 736 and 720 unobscured and obscured X-ray-selected AGNs (0.5–8 keV) with column densities higher and lower than $N_{\rm H} = 10^{22}\,{\rm cm}^{-2}$, respectively. We perform a spatial correlation function analysis for the two samples, and we find a weak (2σ) difference in the clustering of obscured sources ($r_{\rm o} = 7.0 \pm 0.6\,h^{-1}$ Mpc) compared to that of unobscured sources ($r_{\rm o} = 5.4 \pm 0.6\,h^{-1}$ Mpc) using a fixed slope of $\gamma = 1.8$. Furthermore, we compare our findings with recent results that base the obscured and unobscured AGN classification on the optical/IR colour ($R - [4.5] = 6.1$). We find that the optical/IR criterion fails to identify a purely AGN sample. In particular, reddened AGNs with $R - [4.5] > 6.1$ are divided almost equally between X-ray obscured and unobscured AGNs. Derivation of the spectral energy distributions reveals that in many cases the host galaxy contaminates the mid-IR bands thus affecting the optical/mid-IR obscured AGN classification.

Key words: galaxies: active – X-rays: galaxies.

1 INTRODUCTION

Some classes of active galactic nuclei (AGNs) belong to the most luminous sources in the Universe. Their luminosity originates from the accretion of matter on to the central supermassive black hole (SMBH). However, the physical mechanism responsible for this accretion still remains unclear. A plausible trigger of accretion on to SMBH that has attracted much attention in the literature are major mergers and more generically galaxy interactions (Hopkins et al. 2005, 2006, 2008a). However, moderate luminosity AGNs ($\log L/({\rm erg\,s^{-1}}) < 44$) can be triggered by an alternative process such as accretion from the hot halo itself (Fanidakis 2012). The above triggering mechanisms may affect the morphology of host galaxy and the appearance of AGNs as obscured or unobscured.

According to the unification models (Antonucci 1993; Urry & Padovani 1995), all AGNs are intrinsically identical. The appearance as Type 1 and Type 2 AGNs can be explained by the orientation of an obscuring torus, around the accretion disc which feeds the black hole, with respect to the line of sight of the observer. For that reason, the classification of AGNs as obscured or unobscured AGN can be explained by geometrical effects.

However, there could be intrinsic physical differences or different AGN feedback models (i.e. major mergers, disc instabilities) that can explain the obscuration through evolutionary effects. At $z > 1$, the obscuration could be caused by major mergers (Hopkins et al. 2008a; Kocevski et al. 2015; Ricci et al. 2017), whereas at lower redshifts disc instabilities could trigger the obscured phase of AGNs (Hopkins et al. 2008b). In these models, the AGN emission is obscured by host galaxy dust and obscuration represents an early evolutionary stage of rapid black hole growth that is also accompanied by a short-term quenching of star formation.

In a recent study, Koulouridis (2014) examined the local environment ($< 200\,h^{-1}$ kpc) of Seyfert 2 galaxies and found indications that heavily obscured objects represent an evolutionary sequence of activity triggered by close galaxy interactions and merging. At a later stage, geometrical effects (i.e. the standard unification model) can explain successfully the classification of AGNs in Type 1 and Type 2. Based on the above, the classification of AGNs in terms

★ E-mail: lazkoutou@gmail.com (LK); ig@noa.gr (IG);gmoun@noa.gr (GM)

of obscuration properties is the combination of both evolutionary and geometrical effects. The study of the large-scale structure and specifically the clustering of AGNs provides a robust statistical tool to test the above hypothesis. If obscuration is an orientation effect then we expect obscured and unobscured AGNs to have similar clustering. Different clustering implies that the two populations live in different environments and this favours the evolutionary scenario.

Several studies have attempted to estimate the duty cycle of the AGNs (Croom et al. 2005; Ebrero et al. 2009; Gilli et al. 2009; Cappelluti et al. 2010). Their estimated values range from 10^7 to 10^9 yr. In any case, the lifetimes of AGNs are significantly shorter than the halo's lifetime which to a first approximation corresponds to the Hubble time at redshift z (Martini & Weinberg 2001). A difference in the clustering amplitude for obscured and unobscured AGNs is expected in some evolutionary scenarios. DiPompeo et al. (2014) performed an abundance matching analysis and estimated the lifetimes for both obscured and unobscured quasar of the order of a few 100 Myr. They mentioned however that the obscured phase is of the order a few times longer than the unobscured phase. Although a number of studies have attempted to compare the clustering of obscured and unobscured X-ray AGNs, the results are inconclusive. In particular, Coil et al. (2009) examined the clustering of X-ray-selected AGNs from the AEGIS survey in the redshift interval $0.7 < z < 1.4$, selecting obscured and unobscured sources based on their hardness ratio (HR). They concluded that there is no significant difference in the clustering of the two populations. This result has also been confirmed by Gilli et al. (2009), which analysed data from the *XMM*-COSMOS field. Mountrichas & Georgakakis (2012) performed a cross-correlation analysis using data from the *XMM*-SDSS survey in the local Universe and found no statistically significant dependence of clustering on obscuration. Performing an angular correlation analysis, Ebrero et al. (2009) found no differences in the clustering between sources with high and those with low HR.

At higher redshifts ($z < 4$ and $2.2 < z < 6.8$), Allevato et al. (2011, 2014) performed a spatial clustering analysis in the *XMM*-COSMOS field and found that unobscured X-ray AGNs reside in more massive haloes than their obscured counterparts. Prompted by the fact that both obscured and unobscured AGNs can be misclassified in spectroscopic studies, due to the host galaxy light that may outshine the nuclear emission, they classified their sources into obscured and unobscured using a combination of X-ray and optical criteria. They suggest that theoretical models that assume a quasar phase triggered by major mergers cannot reproduce the high bias factors found for unobscured AGN, indicating that unobscured X-ray AGN constitutes a different family of AGNs.

Differences in the clustering of obscured and unobscured X-ray AGNs were also found by Elyiv et al. (2012). Measuring the two-point correlation function in the *XMM*-LSS survey found that AGN sources in the hard band (2–10 keV) are more clustered than sources in the soft band (0.5–2 keV). They concluded that this result may be a hint that the obscured AGN populate in different environment than unobscured AGN.

A series of recent studies that performed spatial (Hickox et al. 2011) or angular (DiPompeo et al. 2014; Donoso et al. 2014; DiPompeo, Hickox & Myers 2016) clustering analysis of infrared (IR)-selected AGNs at $z \sim 1$, found that obscured AGNs appear to be clustered more strongly than unobscured AGNs. In these studies, though, the classification into obscured and unobscured IR sources is based on the observed optical to mid-IR colour cut.

Recently Mendez et al. (2016) measured the spatial clustering of X-ray, radio, and mid-IR-selected AGNs at $0.2 < z < 1.2$ from the PRIMUS and DEEP2 redshift surveys. They classified their sources based on obscuration using an optical to IRAC colour cut and found no significant dependence of the clustering on obscuration. They state that the different clustering results found from the above IR studies are due to cosmic variance and sample selection effects (redshift distribution).

The general picture from the above studies investigating the clustering dependence on obscuration remains unclear. In this work, we investigate anew, the dependence of clustering on obscuration, using one of the largest samples of X-ray AGNs, compiled from 1456 X-ray AGNs with spectroscopic redshifts. Throughout this paper, we adopt a flat ΛCDM model with $\Omega_m = 0.3$ and $H_0 = 100\,\mathrm{km\,s^{-1}\,Mpc^{-1}}$.

Table 1. Number of X-ray sources with spectroscopic redshifts available in each field.

Field	Area (deg^2)	No. of S (with spec-z)	
CDF-N	0.12	128	Xue et al. (2016)
CDF-S(7Ms)	0.13	159	Luo et al. (2017)
ECDF-S	0.31	114	Xue et al. (2016)
AEGIS	0.67	285	Davis et al. (2001, 2003), Coil et al. (2009), Nandra et al. (2015)
COSMOS	2.2	770	Marchesi et al. (2016)

2 AGN CATALOGUES

In order to perform a spatial two-point autocorrelation analysis, we combine five *Chandra* fields, CDF-N, CDF-S, ECDF-S, COSMOS, and AEGIS (Alexander et al. 2003; Nandra et al. 2015; Civano et al. 2016; Xue et al. 2016; Luo et al. 2017, see also Koutoulidis et al. 2013), in the full band 0.5−8 keV, using in total 1456 X-ray AGNs. All these sources have spectroscopic redshifts available (see Table 1).

The whole X-ray AGN sample is limited in the redshift interval $z = 0.6-1.4$, a range that contains the bulk of AGNs, while minimizing the contribution of clustering evolution with redshift. In order to avoid the contamination of our X-ray AGN sample by normal galaxies, we use sources with absorption corrected (i.e. intrinsic in 0.5−10 keV energy band) $L_x > 10^{42}\,\mathrm{erg\,s^{-1}}$.

3 METHODOLOGY

3.1 Theoretical considerations

The correlation function provides a means to characterize the structure of matter distribution in the Universe. The two-point correlation function, which describes the excess probability above a random distribution of finding pairs of sources within a range of separations, is the low-order clustering and the simplest probe of the distribution of sources.

The derivation of the spatial correlation function, $\xi(r)$, is based on the knowledge of observed redshifts. The relative velocities of extragalactic sources are not only due to Hubble expansion but they are contaminated by local peculiar velocities. Due to these peculiar velocities the observed redshift of the source is the superposition of the cosmic expansion velocity and its peculiar velocity along the line of sight. An estimator to overcome the influence of non-

negligible peculiar velocities is the projected correlation function $w_p(r_p)$ (e.g. Davis & Peebles 1983). Using this estimator we can infer the spatial clustering, which is not hampered by the effects of z-distortions. This estimator is based on deconvolving the redshift-based distance of a source, s, in two components, one parallel (π) and one perpendicular (r_p) to the line of sight, i.e. $s = (r_p^2 + \pi^2)^{1/2}$, and thus the redshift-space correlation function can be written as $\xi(s) = \xi(r_p, \pi)$. Since redshift-space distortions affect only the π component, one can estimate the free of z-space distortions projected correlation function, $w_p(r_p)$, by integrating $\xi(r_p, \pi)$ along π:

$$w_p(r_p) = 2\int_0^\infty \xi(r_p, \pi)\mathrm{d}\pi. \quad (1)$$

Once we estimate the projected correlation function, $w(r_p)$, we can recover the real space correlation function, since the two are related according to Davis & Peebles (1983) formula:

$$w_p(r_p) = 2\int_0^\infty \xi\left(\sqrt{r_p^2+\pi^2}\right)\mathrm{d}\pi = 2\int_{r_p}^\infty \frac{r\xi(r)\mathrm{d}r}{\sqrt{r^2-r_p^2}}. \quad (2)$$

Modelling $\xi(r)$ as a power law: $\xi(r) = (r/r_0)^{-\gamma}$ one obtains:

$$w_p(r_p) = A_\gamma r_p\left(\frac{r_0}{r_p}\right)^\gamma, \quad (3)$$

with r_0 the comoving clustering length at the effective redshift of the sample

$$A\gamma = \Gamma\left(\frac{1}{2}\right)\Gamma\left(\frac{\gamma-1}{2}\right)/\Gamma\left(\frac{\gamma}{2}\right). \quad (4)$$

However, it should be noted that equation (3) strictly holds for $\pi_{\max} = \infty$ and therefore imposing a cutoff $\pi_{\max}$ introduces an underestimation of the underlying correlation function, which is an increasing function of separation r_p. For a power-law correlation function, this underestimation is easily inferred from equation (2) and is given by (Starikova et al. 2011)

$$C_\gamma(r_p) = \frac{\int_0^{\pi_{\max}}(r^2+\pi^2)^{-\gamma/2}\mathrm{d}\pi}{\int_0^\infty(r^2+\pi^2)^{-\gamma/2}\mathrm{d}\pi}. \quad (5)$$

Thus, taking into account the above statistical correction and under the assumption of the power-law correlation function, one can recover the corrected spatial correlation function, $\xi(r_p)$, from the measurement of $w_p(r_p)$ and its fit (which provides the value of γ), according to

$$\xi(r_p) = \frac{1}{A_\gamma C_\gamma(r_p)}\frac{w_p(r_p)}{r_p}. \quad (6)$$

However, at large separations, the correction factor increasingly dominates over the signal and thus it constitutes the correction procedure unstable. For the purpose of this work, we will derive a power-law fit of $\xi(r_p)$ but only within $1 < r_p < 10\,h^{-1}$ Mpc. Alternatively, one can estimate crudely the corrected spatial correlation length by using the following scaling:

$$r_{0,c} = r_0 C_\gamma(r_0)^{-1/\gamma}, \quad (7)$$

where r_0 and γ are derived from fitting the data to equation (3).

3.2 Correlation function estimator

For the estimation of the correlation function, various estimators have been used in the literature. For a comparison among them, see Kerscher, Szapudi & Szalay (2000) and Plionis et al. (2018). In our analysis, we use the Landy & Szalay (1993) that has the smallest scatter in the clustering measurements.

$$1+\xi(r_p,\pi) = \frac{DD(r_p,\pi) - 2DR(r_p,\pi) + RR(r_p,\pi)}{RR(r_p,\pi)}, \quad (8)$$

where $DD(r_p, \pi)$, $RR(r_p, \pi)$, and $DR(r_p, \pi)$ are the number of data–data, random–random, and data–random pairs, respectively.

Then, the redshift-space correlation function, $\xi(s)$, is estimated in the range $s = 1-30\,h^{-1}$ Mpc and the projected correlation function, $w_p(r_p)$, along the r_p direction (equation 2) in the separation range $r_p = 0.16-30\,h^{-1}$ Mpc. Note that large separations in the π direction add mostly noise to the above estimator and therefore the integration is truncated for separations larger than $\pi_{\max}$, the choice of which is a compromise in having an optimal signal-to-noise ratio for ξ while reducing the excess noise from high π separations. Different studies have used the range $\pi_{\max} \in [5, 30]\,h^{-1}$ Mpc.

The correlation function uncertainty is estimated according to

$$\sigma_{w_p} = \sqrt{3}(1+w_p)/\sqrt{DD}, \quad (9)$$

which corresponds to that expected by the bootstrap technique (Mo & White 1996). Then using a χ^2 minimization procedure between data and the power-law model for either type of the correlation function, we derive the best-fitting r_0 and γ parameters. We use only large separations (i.e. $r_p > 1\,h^{-1}$ Mpc) in order to minimize the non-linear effects, and a range in which a power-law model can be fitted with relatively good accuracy.

4 RESULTS

4.1 Obscuration

For the classification of X-ray AGNs as obscured or unobscured, we make use of the X-ray colour indices (HR). HR is not as reliable as X-ray spectroscopy, but can be used as an approximate method to classify obscured and unobscured sources. HR is defined as $HR = (H - S)/(H + S)$, where H and S are the observed counts in the hard 2−7 keV and the soft 0.5−2 keV bands, respectively. Then we compare these HR values with a power-law model assuming $N_H = 10^{22}\,\mathrm{cm}^{-2}$ at the redshift interval $0.6 < z < 1.4$. Using this approach in all the examined fields, we obtain 736 X-ray obscured and 720 X-ray unobscured sources (Fig. 1). Applying the luminosity cut mentioned above (i.e. $\log L_x > 42$), the median X-ray luminosity of the 736 obscured AGN sample, which covers a range of $42.01 \le \log L_x \le 44.98$, is $\mathbf{log}\,\bar{L}_x = 43.06$, while for the 720 unobscured AGN sample which covers a range of $42.01 \le \log L_x \le 45.27$ is $\log \bar{L}_x = 43.24$.

The construction of the random catalogue follows the procedure described in Gilli et al. (2005) for each field separately and then combining all the fields to construct a total sample of obscured and unobscured sources.

In order to estimate the two-point spatial correlation function we must examine the redshift distributions for both unobscured and obscured X-ray AGNs in order to avoid any evolution of the correlation function with redshift. Fig. 2 presents the redshift distribution of obscured and unobscured AGNs. Both populations have similar redshift distributions and therefore we do not expect any dependence of the clustering length on redshift.

As mentioned in Section 3, the correlation functions are fitted in scales $r_p = 1$–$10\,h^{-1}$ Mpc. In Fig. 3, we present for both obscured and unobscured X-ray sources the clustering length $r_{p,0}$ as a function of $\pi_{\max}$ for fixed slope $\gamma = 1.8$. The clustering signal saturates and the uncertainties minimize for $\pi_{\max} = 20\,h^{-1}$ Mpc. At smaller

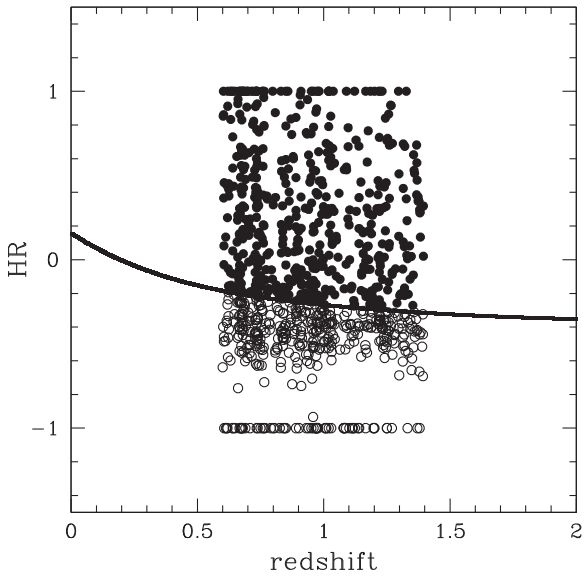

Figure 1. The X-ray HR. Due to the fact that the examined sample of AGN span at redshift $0.6 < z < 1.4$, we derived the HR as a function of redshift, assuming $N_{\rm H} = 10^{22}\,{\rm cm}^{-2}$ for photon index $\Gamma = 1.8$ (black continuous line). Filled black circles represent obscured X-ray AGN and open circles represent unobscured X-ray AGN.

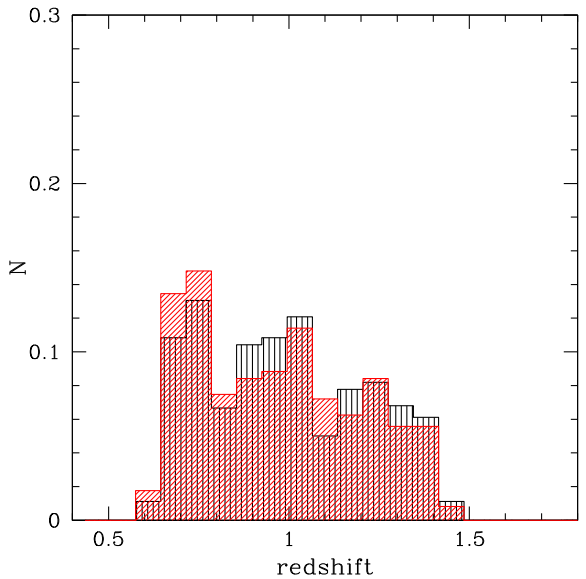

Figure 2. Redshift distributions of unobscured X-ray AGN (black shaded region) and obscured X-ray AGN (red shaded region). Both distributions are normalized to unity.

scales the signal is underestimated and at larger scales the noise is increased. Our best-fitting values for r_0 and γ are estimated using $\pi_{\rm max} = 20\,h^{-1}$ Mpc.

Clustering results for the projected correlation function $w_{\rm p}(r_{\rm p})$ for the obscured and unobscured sources are shown in Fig. 4 . The filled circular points represent those measurements that have been used to fit the power-law model (black solid line). The red dashed line shows the power-law fit for a fixed slope $\gamma = 1.8$. The corresponding best-fitting values for the slope γ and the correlation length are shown in Table 2. Based on our analysis, the correlation length of obscured

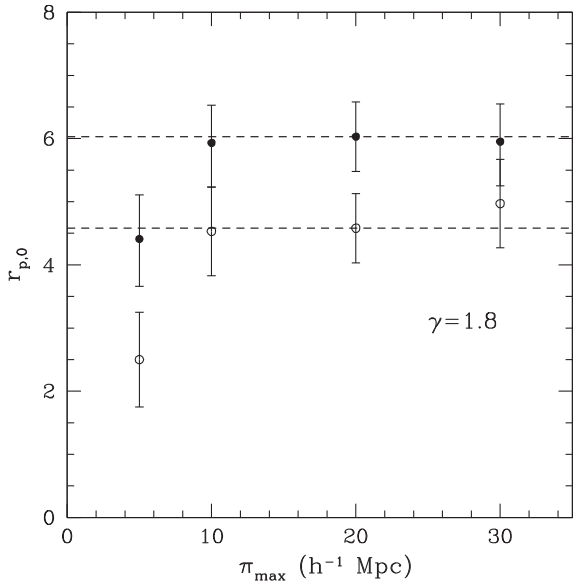

Figure 3. The dependence clustering length on the cutoff $\pi_{\rm max}$ value, for the case of constant slope $\gamma = 1.8$. The black filled points correspond to the derived correlation lengths of obscured sources as a function of $\pi_{\rm max}$, while the open points to the corresponding for unobscured sources. The two dashed lines correspond to the estimated final $r_{\rm p,0}$ correlation lengths of the obscured and unobscured sources, respectively.

and unobscured sources are in statistical agreement and therefore the clustering of the two populations is similar.

5 COMPARISON WITH IR SELECTION OF OBSCURED AGN

Based on the bimodal distribution of IR-selected AGNs in optical to mid-IR colours, Hickox et al. (2007, 2011) classify AGNs into obscured and unobscured using the optical cut $R - [4.5] = 6.1$, where R and [4.5] are the Vega magnitudes in the R and IRAC 4.5 μm bands, respectively. To verify their selection criterion, they also perform an X-ray stacking analysis. They found that IR AGNs Type 1 have HRs consistent with unabsorbed AGN, and the IR AGNs 2 correspond to absorbed sources with $N_{\rm H} = 3 \times 10^{22}\,{\rm cm}^{-2}$. The flux at 4.5 μm corresponds to the flux from the torus which is expected to have a peak at 4−10 μm. If the AGNs have $R - [4.5] > 6.1$ then will have a suppressed optical emission and enhanced torus emission suggesting obscuration.

To further investigate this trend we apply (Hickox et al. 2011) IR criterion in our X-ray sample. Towards this end, we cross-match our X-ray catalogue with the IR/optical catalogues (Capak et al. 2007; Ilbert, Capak & Salvato 2009; Ashby et al. 2015; Nandra et al. 2015; Marchesi et al. 2016; Xue et al. 2016). There is colour information for 573 obscured X-ray AGNs with median redshift $\bar{z} = 1.01$ and for 574 unobscured X-ray AGNs with median redshift $\bar{z} = 0.82$. To compare with the $R - [4.5]$ criterion we transform these magnitudes to Vega system magnitude.

Using the Hickox et al. (2011) criterion, we create two subsamples and estimate their correlation functions. The corresponding best-fitting values for the slope γ and the correlation length are shown in Table 3.

Our results reveal an opposite trend, in the sense that unobscured sources appear to be more clustered than obscured sources. In order to investigate in detail this discrepancy, we plot the histogram of

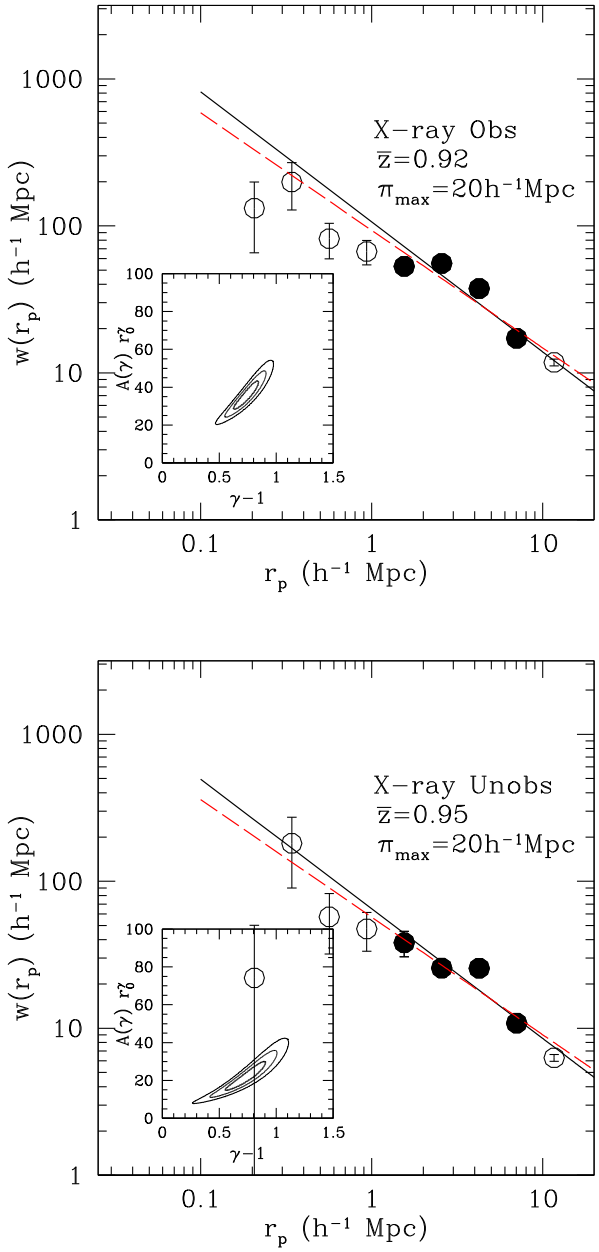

Figure 4. The projected correlation function, $w_p(r_p)$, for the obscured (upper panel) and unobscured X-ray AGNs (lower panel). Only the filled circles are considered in the fitting, indicate the range over which a power-law fit was applied (black line corresponds to a fit with free γ, while the red line to that for $\gamma = 1.8$). The inset panel shows 1σ, 2σ, and 3σ likelihood contours in the two-parameter plane of power-law solutions.

Table 2. Clustering results for the obscured (736) and unobscured (720) X-ray AGN sources. The clustering length units are h^{-1} Mpc. The results correspond to $\pi_{max} = 20\,h^{-1}$ Mpc.

Unobscured AGN	γ	r_0	r_0 ($\gamma = 1.8$)
$w_p(r_p)$	1.88 ± 0.06	4.8 ± 0.4	4.6 ± 0.5
$\xi(r_p)$	1.73 ± 0.20	5.4 ± 0.6	5.4 ± 0.6
Obscured AGN	γ	r_0	r_0 ($\gamma = 1.8$)
$w_p(r_p)$	1.88 ± 0.04	6.2 ± 0.4	6.0 ± 0.5
$\xi(r_p)$	1.74 ± 0.11	7.1 ± 0.6	7.0 ± 0.6

Table 3. Clustering results for the obscured (573) and unobscured (574) X-ray AGN sources according to $R - [4.5]$ criterion. The clustering length units are h^{-1} Mpc. The results correspond to $\pi_{max} = 20\,h^{-1}$ Mpc.

Unobscured AGN	γ	r_0	r_0 ($\gamma = 1.8$)
$w_p(r_p)$	1.68 ± 0.04	6.4 ± 0.5	6.7 ± 0.5
$\xi(r_p)$	1.58 ± 0.20	8.3 ± 0.8	7.2 ± 0.6
Obscured AGN	γ	r_0	r_0 ($\gamma = 1.8$)
$w_p(r_p)$	1.92 ± 0.06	4.7 ± 0.5	4.4 ± 0.5
$\xi(r_p)$	1.76 ± 0.16	5.4 ± 0.7	5.4 ± 0.7

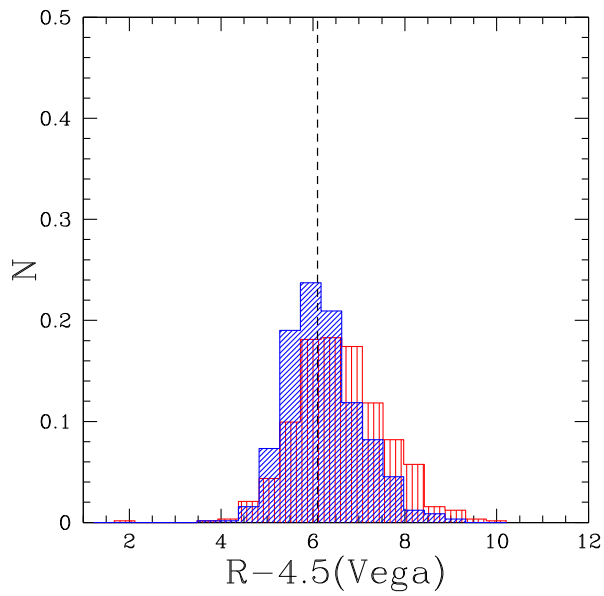

Figure 5. Histogram of $R - [4.5]$ for X-ray unobscured (blue shaded region) and X-ray obscured (red shaded region). The dashed vertical line represents the division line i.e. $R - [4.5] = 6.1$ between obscured and unobscured.

$R - [4.5]$ for X-ray unobscured (blue shaded region) and X-ray obscured (red shaded region) (Fig. 5). Although we observe a slight prevalence for mid-IR obscured AGNs to be obscured in X-rays there is an overlapping region which suggests that there is no one to one correspondence between the two colour cut criteria. Specifically, from 574 X-ray unobscured AGNs, 340 AGNs according to IR/optical criterion are in very good agreement with the HR criterion. However, 234 AGNs according to IR/optical colour cut are classified as obscured (i.e. $R - [4.5] > 6.1$) but are unobscured according to HR classification.

The same trend exists for 573 X-ray obscured AGNs from which 342 according to IR/optical colour cut selection are in very good agreement, but 231 AGNs according to IR/optical colour cut are classified as unobscured (i.e. $R - [4.5] <= 6.1$). It is evident that ~40 per cent of our X-ray sources for both obscured and unobscured AGNs are not in good agreement with the IR/optical colour classification. This explains the reason differences are found in clustering results for obscured and unobscured AGNs according to the mid-IR classification.

5.1 SED fitting

Prompted by the results of the previous section that different obscuration criteria may lead to different classification of a source, we perform a spectral energy decomposition (SED) analysis. The

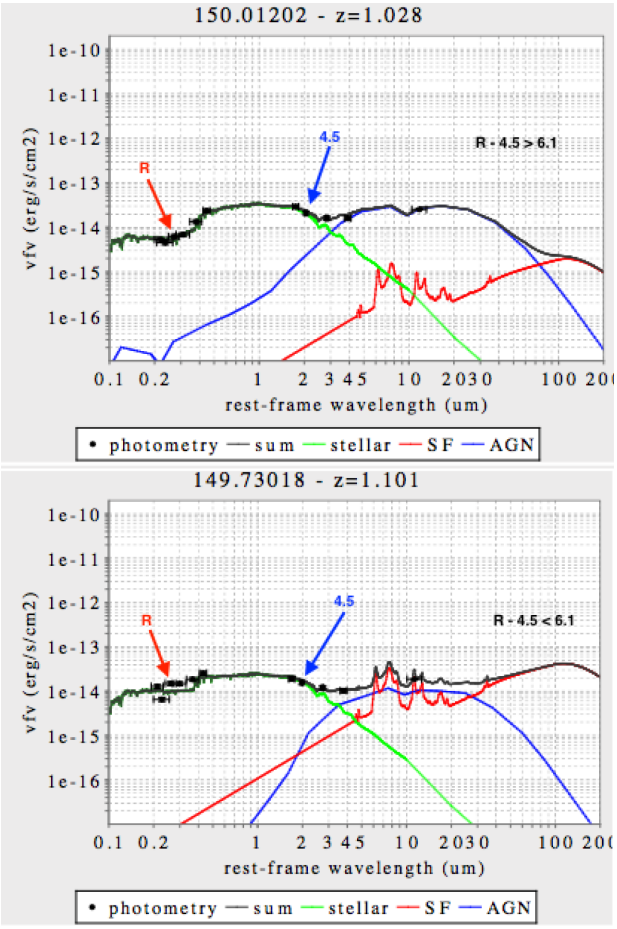

Figure 6. Examples of the best-fitting SEDs (black solid line) in the rest frame of source from Cosmos field. The source is fitted using an AGN component (blue line) with an empirical stellar component (green line) and empirical starburst templates (red line). The source ($\log L_x = 43.7$) in the upper panel is classified as obscured in X-ray and also obscured according to IR colour cut criterion. The source ($\log L_x = 43.3$) in the lower panel is classified as obscured in X-ray but as unobscured according to IR colour cut criterion.

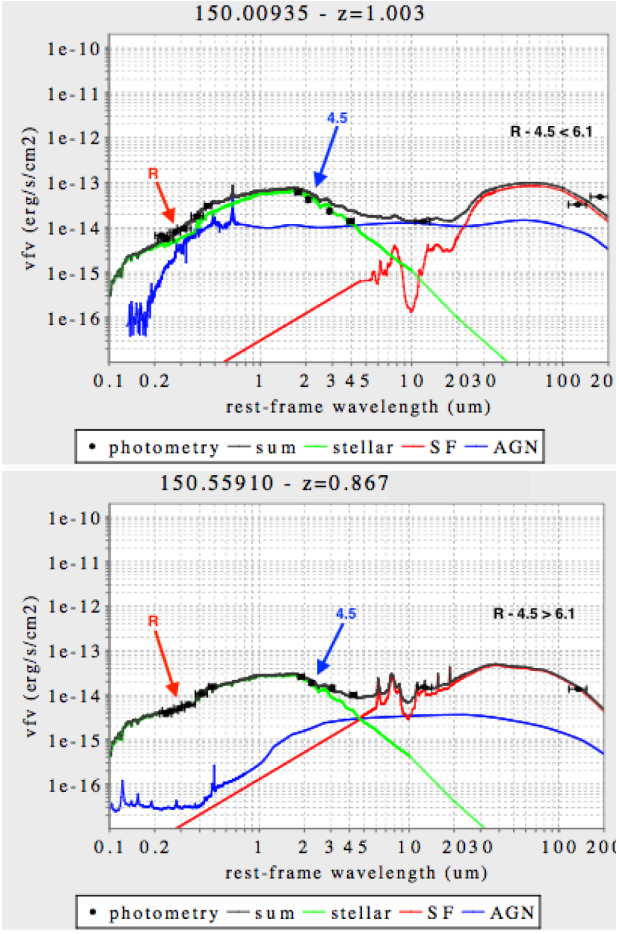

Figure 7. Examples of the best-fitting SEDs (black solid line) in the rest frame of source from Cosmos field. The source is fitted using an AGN component (blue line) with an empirical stellar component (green line) and empirical starburst templates (red line). The source ($\log L_x = 43.2$) in the upper panel is classified as unobscured in X-ray and also in IR colour cut criterion. The source ($\log L_x = 43.4$) in the lower panel is classified as unobscured in X-ray but as obscured in IR colour cut criterion.

SED analysis can disentangle the emission that comes from the host galaxy and the nuclear region. If there is contamination from the emission of the host galaxy, this would affect the IR/optical colour cuts and may explain the reasons of the discrepancy.

For that purpose, we use the AGNs in the C-COSMOS field. The C-COSMOS offers a manageable number of X-ray sources, with available broad-band photometry that covers a wavelength range from optical to far-IR. Our analysis is based on maximum likelihood, using the SEABASS SED fitting code (for details see appendix A, Rovilos et al. 2014). Empirically derived templates are used to disentangle the emission of the host galaxy from that of the nuclear region (Chary & Elbaz 2001; Silva, Maiolino & Granato 2004; Polletta et al. 2007). In the general case, we have three sets of templates code-named, 'stellar', 'SB', and 'AGN', which correspond to stellar, star formation, and AGN emission, respectively.

Based on the HR criterion, 313 AGNs are obscured and 457 unobscured in the COSMOS field. We cross-match these two subsamples with the IRAC (Ilbert et al. 2009) and MIPS24 (McCracken et al. 2010) catalogues of *Spitzer*, the PACS sample of *Herschel* (Lutz et al. 2011), the SPIRE data set (Oliver et al. 2012) as well as the optical catalogue of Capak et al. (2007).

In the case of obscured X-ray AGN, when the blue bump is missing in the UV region due to absorption (Fig. 6, upper panel), IR/optical criteria agree with the X-ray criteria in the characterization of the source as obscured. However, when the stellar component that comes from the host galaxy has higher flux than the nuclear mission (green line; Fig. 6, lower panel), the IR/optical criterion fails to classify the source as obscured. In the case of unobscured X-ray AGN, the blue bump is prominent (Fig. 7, upper panel) and the IR/optical criteria have a higher success rate. Nevertheless, when the host galaxy has higher flux than the flux of the central region (Fig. 7, lower panel), the IR/optical colour cuts classify the AGNs as obscured.

6 SUMMARY AND CONCLUSIONS

We use X-ray AGN in five fields, i.e. CDFN, CDFS, AEGIS, C-COSMOS, and ECDFS fields, to study the environment of obscured and unobscured sources. Our sample consists of 1456 sources, and is one of the largest X-ray samples used to study the dependence of

the clustering on obscuration. Utilizing data from different fields, also minimizes the cosmic variance effect.

Our analysis shows a hint that obscured X-ray AGNs are more clustered than unobscured X-ray AGNs ($r_0 = 7.0 \pm 0.6\,h^{-1}$ Mpc, $r_0 = 5.4 \pm 0.6\,h^{-1}$ Mpc, respectively). However, the difference is statistical insignificant which suggests that the two populations live in similar environments. This is in agreement with the findings of other X-ray studies, at similar and lower redshifts ($z \leq 1$; e.g. Coil et al. 2009; Mountrichas & Georgakakis 2012, but see also Allevato et al. 2011, 2014). The majority of IR-selected AGNs clustering studies find that obscured sources live in more massive haloes than unobscured sources (Hickox et al. 2011; DiPompeo et al. 2014, 2016; Donoso et al. 2014). A theoretical explanation is that if obscured sources live in more dense environments then their black holes are undermassive, i.e. the black hole mass growth lags behind that of the hosting halo (King 2010; Hickox et al. 2011). In this scenario, obscured AGNs represent an early evolutionary stage of rapid black hole growth, before the emergence of an unobscured AGNs (Donoso et al. 2014). However, Mendez et al. (2016) used IR-selected AGNs from seven separate fields, and found the same clustering for obscured and unobscured sources. They claim that the different clustering found by Donoso et al. (2014), which used *WISE* IR-AGN, are due to a flatter redshift distribution and peak of the unobscured AGNs compared to obscured (but see DiPompeo et al. 2016).

The general conclusion from all the above studies is that different wavelengths may select different types of host galaxies and perhaps a specific time in AGN evolution (e.g. Donoso et al. 2014; Mendez et al. 2016; Ballantyne 2017). Our SED analysis shows that optical/IR selection criteria for obscured and unobscured X-ray AGNs found a mixture of objects. The SED decomposition performed revealed that the cause of this discrepancy may be due to the contamination of the emission from the host galaxy that is hard to disentangle from the nuclear region and affects the optical colour cut criteria.

ACKNOWLEDGEMENTS

The authors are grateful to the anonymous referee for helpful comments that helped to improve this paper substantially. GM acknowledges financial support from the AHEAD project, which is funded by the European Union as Research and Innovation Action under Grant No. 654215.

REFERENCES

Alexander D. M. et al., 2003, AJ, 126, 539
Allevato V. et al., 2011, ApJ, 736, 99
Allevato V. et al., 2014, ApJ, 796, 4
Antonucci R., 1993, ARA&A, 31, 473
Ashby M. L. N. et al., 2015, ApJS, 218, 33
Ballantyne D. R., 2017, MNRAS, 464, 626
Capak P., Aussel H., Ajiki M., McCracken H. J., Mobasher B., Scoville N., Shopbell P., 2007, ApJS, 172, 99
Cappelluti N., Ajello M., Burlon D., Krumpe M., Miyaji T., Bonoli S., Greiner J., 2010, ApJ, 716, L209
Chary R., Elbaz D., 2001, ApJ, 556, 562
Civano F., Marchesi S., Comastri A., Urry M. C., Elvis M., Cappelluti N., 2016, ApJ, 819, 62
Coil A. L. et al., 2009, ApJ, 701, 1484
Croom S. M. et al., 2005, MNRAS, 356, 415
Davis M., Peebles P. J. E., 1983, ApJ, 267, 465
Davis M., Newman J. A., Faber S. M., Phillips A. C., 2001, in Cristiani S., Renzini A., Williams R. E., eds, Deep Fields The DEEP2 Redshift Survey. Springer-Verlag, Berlin, p. 241
Davis M. et al., 2003, in Guhathakurta P., ed., Proc. SPIE Conf. Ser. Vol. 4834, Science Objectives and Early Results of the DEEP2 Redshift Survey. SPIE, Bellingham, p. 161
DiPompeo M. A., Myers A. D., Hickox R. C., Geach J. E., Hainline K. N., 2014, MNRAS, 442, 3443
DiPompeo M. A., Hickox R. C., Myers A. D., 2016, MNRAS, 456, 924
Donoso E., Yan L., Stern D., Assef R. J., 2014, ApJ, 789, 44
Ebrero J., Mateos S., Stewart G. C., Carrera F. J., Watson M. G., 2009, A&A, 500, 749
Elyiv A. et al., 2012, A&A, 537, A131
Fanidakis N., Baugh C. M., Benson A. J., Bower R. G., Cole S., Done C., Frenk C. S., 2012, MNRAS, 419, 2797
Gilli R. et al., 2005, A&A, 430, 811
Gilli R. et al., 2009, A&A, 494, 33
Hickox R. C. et al., 2007, ApJ, 671, 1365
Hickox R. C., Myers A. D., Brodwin M., Alexander D. M., 2011, ApJ, 731, 117
Hopkins P. F., Hernquist L., Cox T. J., Di Matteo T., Robertson B., Springel V., 2005, ApJ, 630, 716
Hopkins P. F., Hernquist L., Cox T. J., Di Matteo T., Robertson B., Springel V., 2006, ApJ, 163, 1
Hopkins P. F., Hernquist L., Cox T. J., Kereš D., 2008a, ApJS, 175, 356
Hopkins P. F., Cox T. J., Kereš D., Hernquist L., 2008b, ApJS, 175, 390
Ilbert O., Capak P., Salvato M., 2009, ApJ, 690, 1236
Kerscher M., Szapudi I., Szalay A. S., 2000, ApJ, 535, L13
King A. R., 2010, MNRAS, 408, L95
Kocevski D. D. et al., 2015, ApJ, 814, 104
Koulouridis E., 2014, A&A, 570, A72
Koutoulidis L., Plionis M., Georgantopoulos I., Fanidakis N., 2013, MNRAS, 428, 1382
Landy S. D., Szalay A. S., 1993, ApJ, 412, 64
Luo B., Brandt W. N., Xue Y. Q., Lehmer B., Alexander D. M., 2017, ApJS, 228, 2
Lutz D. et al., 2011, A&A, 532, A90
Marchesi S., Civano F., Elvis M., Salvato M., Brusa M., Comastri A., 2016, ApJ, 817, 34
Martini P., Weinberg D. H., 2001, ApJ, 547, 12
McCracken H. J. et al., 2010, ApJ, 708, 202
Mendez A. J. et al., 2016, ApJ, 821, 55
Mo H. J., White S. D. M., 1996, MNRAS, 282, 347
Mountrichas G., Georgakakis A., 2012, MNRAS, 420, 514
Nandra K., Laird E. S., Aird J. A., Salvato M., Georgakakis A., 2015, ApJS, 220, 10
Oliver S. J. et al., 2012, MNRAS, 424, 1614
Plionis M. et al., 2018, preprint (arXiv:1804.06409)
Polletta M., Tajer M., Maraschi L., Trinchieri G., Lonsdale C. J., Chiappetti, 2007, ApJ, 663, 81
Ricci C. et al., 2017, MNRAS, 468, 1273
Rovilos E. et al., 2014, MNRAS, 438, 494
Silva L., Maiolino R., Granato G. L., 2004, MNRAS, 355, 973
Starikova S. et al., 2011, ApJ, 741, 15
Urry C. M., Padovani P., 1995, PASP, 107, 803
Xue Y. Q., Luo B., Brandt W. N., Alexander D. M., Bauer F. E., Lehmer B. D., Yang G., 2016, ApJS, 224, 15

This paper has been typeset from a TEX/LATEX file prepared by the author.